Lattice Boltzmann study of miscible viscous fingering for binary and ternary mixtures

Lucien Vienne, Simon Marié

Lattice Boltzmann study of miscible viscous fingering for binary and ternary mixtures

Lucien Vienne [1,2,*] and Simon Marié [1,†]

[1] *Laboratoire DynFluid, Conservatoire National des Arts et Métiers, 151 boulevard de l'hôpital, 75013 Paris, France*

[2] *Laboratoire de Mécanique des Fluides et d'Acoustique, École Centrale de Lyon, 69134 Écully, France*

(Received 30 July 2020; accepted 11 May 2021; published 26 May 2021)

A lattice Boltzmann simulation of a viscous fingering instability with miscible components is performed. The core ingredients of the instability are related to the molecular diffusion and the viscosity discrepancy, or, more specifically for the lattice Boltzmann model (LBM), intermolecular friction forces and partial viscosities. Generally, the instability occurs when a less viscous fluid displaces a more viscous fluid in a porous medium. The viscous fingering is first studied in the case of a binary mixture. At early times in the linear regime, the growth rate of the perturbation is computed for different Péclet numbers. The growth rate, as well as the most dangerous and cutoff numbers, increases with the Péclet number. A good agreement is found with a linear stability analysis in which a quasi-steady-state approximation is used. For intermediate times when strong nonlinear interactions take place, the development of the instability is described globally through the mixing length. A high Péclet number leads to more intense instability. Two regimes are visible: the diffusive regime, when fingers remain small and the growth of the mixing length is dominated by diffusion and proportional to $\sqrt{t^\star}$, and the convective regime, when fingers become larger than the diffusive length and the growth of the mixing length is proportional to $t^\star$. Finally, it is shown that the LBM can describe complex diffusion specific to the case of three species. For instance, viscous fingering could be induced by reverse diffusion despite having a stable initial flow configuration. At early times, each species exhibits different growth rates and then converges to the same value. Afterward, the same diffusive and convective regimes are also recovered for the three species but are delayed in time due to the complex diffusion mechanisms.

DOI: 10.1103/PhysRevFluids.6.053904

I. INTRODUCTION

Fluid flows and mixing in porous media play key roles in many real-world engineering problems such as in chromatographic columns, secondary and tertiary oil recovery, carbon dioxide sequestration, and microfluidic devices. Interfacial instabilities can be detrimental for the previous processes or be a way to improve the mixing. High Reynolds number flows can be actively stirred by turbulence but other mechanisms are needed in a porous medium. The generation of an interfacial instability is one mechanism among others that can improve the mixing. This instability can be driven by chemical reactions, density stratification (Rayleigh-Taylor instability), and/or difference in viscosity. Here, we focus on the latter, which is called viscous fingering or Saffman-Taylor instability. This interfacial instability occurs when a less viscous fluid displaces a more viscous

*Corresponding author: contact@lvienne.com

†simon.marie@lecnam.net

fluid in a porous medium [1]. Finger-like patterns emerge and grow, exhibiting complex dynamics. The influence of the instability should not be underestimated. Using data from a CO_2 sequestration project, the mixing zone after a shutdown time of approximately 150 years is estimated to be around 50 km long, whereas it would be roughly 5 m if only pure diffusion is considered [2].

Porous media, such as natural soils or sedimentary rocks, are incredibly difficult to model due to the heterogeneous structure and composition of the pores at many different scales. Since they are opaque, most experimental investigations of the viscous fingering phenomena are carried out on Hele-Shaw cells. A Hele-Shaw cell is composed of two parallel plates with a small gap. This flow configuration mimics the drag induced by a porous medium when the gap is small enough. From a numerical point of view, the simulation of a large-scale flow at the pore scale is often impractical because of long CPU time and excessive memory consumption. Hence, a volume average approach is usually used to overcome these difficulties. In this case, Darcy or Darcy-Brinkman semiempirical equations are solved and porosity, permeability, and other measurements are defined [3].

Since the pioneering work of Hill [4] in 1952 and Saffman and Taylor [5] in 1958, extensive investigations have been performed on both immiscible and miscible viscous fingering. A distinctive characteristic of miscible fluids is the lack of a sharp interface and surface tension. Mixing produces changes in the fluid since the properties of the mixture vary continuously while diffusion occurs. Usually, the viscous fingering is modeled by using Darcy's law and a scalar transport equation for the concentration. A relation between the viscosity and the concentration of the components must be defined. Most articles follow the standard literature rather than physical rigor and assume an exponential dependence.

Studies of the viscous fingering instability can be divided into two categories: linear stability analyses and nonlinear simulations. The linear stability analysis is a classical tool to study the evolution of small perturbations that leads to instability. The main mathematical challenge of the miscible viscous fingering is due to the unsteady base (i.e., unperturbed) state caused by diffusion. In practice, the quasi-steady-state approximation is employed and the linear stability analysis is applied on a frozen base state at successive frozen times [6,7]. Other methods such as initial value problem or nonmodal analysis (transient growth analysis) are possible. Excluding the transient growth at very short times, the different approaches are in good agreement [6,8]. As its name implies, linear stability analyses are restricted to early times. As the perturbation develops, nonlinear interactions occur and the linearized equations are no longer valid. This leads to the second category, nonlinear simulations where no approximation is made and thus the full life cycle of fingers, from onset to shutdown, can be studied. In this case, the governing equations are solved with a stream-function formulation using a spectral method [6,7,9,10] or a finite-difference method [2,11]. The former is very efficient whereas the latter can be numerically stable for any viscosity ratios.

The lattice Boltzmann method (LBM) was also used to study the viscous fingering phenomenon. In 1992, Holme and Rothman [12] proposed a LBM for miscible binary fluids where one distribution function models an advection-diffusion equation and a second distribution function is employed for the mixture density and momentum balance equations. Then, they simulate the viscous fingering instability using their miscible model with a variable mixture viscosity and a drag force that mimics the effect of a porous medium. With a similar miscible LBM approach, Rokotomalala *et al.* [13] studied the miscible displacement of two fluids with different viscosities between two parallel plates. In the absence of a porous medium, a single finger may appear, depending on the diffusion and the viscosity contrast. This can be seen as a limit case of the viscous fingering instability. Lattice Boltzmann simulations (e.g., Refs. [14,15]) are usually applied to pore-scale simulations in which the pore geometry influences the flow. More recently, Lei and Luo [16] examined the dissolution-driven density instability with a reaction at the pore scale. Two remarks can be made regarding the pore-scale representation of the porous medium and the way diffusion is taken into account in lattice Boltzmann models. At pore scale, the geometry of the pores influences the dynamics of the instability. On the other hand, the assumption of a Darcy flow made in the classical literature [1] means that diffusion acts quickly to homogenize flow structures at the pore scale and a global variable as the permeability of the porous medium can be defined. Simulating a Darcy

flow with a lattice Boltzmann model makes it possible here to compare results with the classical (non-LBM-related) literature about the viscous fingering instability. Second, and in contrast to the previous LB simulations where an advection-diffusion equation for the concentration is solved, a more natural approach to deal with diffusion in the frame of the lattice Boltzmann method is the use of an intermolecular friction force [17,18] or a more complex collision model [19–23] to take into account diffusion between species. Indeed, the distribution function for the diffusion equation lost its molecular meaning and is no longer associated with the physical description of a species, i.e., collisions of molecules. More specifically, the diffusion equation is postulated and a kinetic scheme is tailored so as to solve it.

Here, neither transport equation for the concentration nor Darcy equation with exponential viscosity dependency is solved. Each species dynamic is governed by its own kinetic equation where diffusion is taken into account through an intermolecular force and the viscosity of species stemmed from the kinetic theory of gases. Adopting a lattice Boltzmann approach, the porous medium effects are taken into account by the Brinkman force model, adding a drag force to the collision operator. With a different approach employed here, we will first verify if we recover well-known results for the binary viscous fingering. Then, by taking advantage of the multispecies lattice Boltzmann model, we will explore the effects of multicomponent diffusion that can affect the dynamic of the viscous fingering instability.

The structure of the article is organized as follows. In the first section, we present the lattice Boltzmann model used for multiples miscible species and the numerical model used for the porous medium. The second section is dedicated to the numerical simulation of the viscous fingering instability with two and three species.

II. NUMERICAL MODEL

The simulation of the miscible viscous fingering instability in the present study is mainly led by two different aspects. The first one relies on the ability to take into account several components with different viscosity and diffusion properties; the second one is the ability to model the presence of a porous media in the simulation. Both of these steps are overcome by adding a source term in the base equations and are detailed in the following.

A. Multicomponents flows with the lattice Boltzmann method

The lattice Boltzmann method is a specific discretization of the Boltzmann equation [24] and has gained some popularity as an alternative method for simulating fluid flows by solving a simplified formulation of the kinetic model. A natural approach to extend the lattice Boltzmann method to multiple components is to define a distribution function, f_α^m, for each species m. The macroscopic quantities of a mixture composed of N species are given as usual by the moments of the distribution functions, such as the density of the mth species is

$$\rho_m(\boldsymbol{x},t) = \sum_\alpha f_\alpha^m(\boldsymbol{x},t), \quad 1 \leqslant m \leqslant N, \tag{1}$$

and the species momentum is

$$\rho_m(\boldsymbol{x},t)\boldsymbol{u}_m(\boldsymbol{x},t) = \sum_\alpha f_\alpha^m(\boldsymbol{x},t)\boldsymbol{e}_\alpha, \quad 1 \leqslant m \leqslant N, \tag{2}$$

where $\boldsymbol{e}_\alpha$ are the discrete kinetic velocities.

In the case of single-component flows, the Bhatnagar-Gross-Krook (BGK) collision operator (or a similar more advanced collision operator) is often used and captures the relaxation of the distribution function toward an equilibrium state according to a relaxation time. Unfortunately, there is no unique or well-established relaxation collision operator for mixtures. Hence, different lattice Boltzmann methods have been developed depending on the underlying kinetic theory [18–23]. We

use the model proposed in Ref. [18] where the discrete kinetic equation reads

$$f_\alpha^m(\boldsymbol{x}+\boldsymbol{e}_\alpha\delta_t, t+\delta_t) = f_\alpha^m(\boldsymbol{x},t) - \frac{\delta_t}{\tau_m}\left[f_\alpha^m(\boldsymbol{x},t) - f_\alpha^{m(\mathrm{eq})}(\boldsymbol{x},t)\right] + \delta_t\left(1-\frac{\delta_t}{2\tau_m}\right)S_\alpha^m(\boldsymbol{x},t) \quad \text{for } 1\leqslant m\leqslant N. \tag{3}$$

The first line of Eq. (3) is the usual relaxation toward the local species equilibrium state

$$f_\alpha^{m(\mathrm{eq})} = \rho_m\omega_\alpha\left[1+\frac{\boldsymbol{u}_m\cdot\boldsymbol{e}_\alpha}{c_s^2}+\frac{(\boldsymbol{u}_m\cdot\boldsymbol{e}_\alpha)^2}{2c_s^4}-\frac{\boldsymbol{u}_m\cdot\boldsymbol{u}_m}{2c_s^2}\right], \tag{4}$$

where ω_α are the lattice weights and c_s is the pseudospeed of sound. The relaxation process is related to the viscous dissipation of the species. Performing a Chapman-Enskog expansion procedure, one finds that the relaxation time depends on the species viscosities according to

$$\mu_m = \rho_m c_s^2\left(\tau_m - \frac{\delta_t}{2}\right). \tag{5}$$

The species viscosity depends on the molar fraction of the different species composing the mixture, the molar masses, and the pure viscosities (when the species is alone). An analytical approximation of the species viscosity can be obtained via the kinetic theory of gases [17,25], resulting in

$$\mu_m = \frac{x_m\mu_{0,m}}{\sum_n^N x_n\Phi_{mn}}, \tag{6}$$

$$\Phi_{mn} = \frac{1}{2\sqrt{2}}\left(1+\frac{M_m}{M_n}\right)^{-\frac{1}{2}}\left[1+\left(\frac{\mu_{0,m}}{\mu_{0,n}}\right)^{\frac{1}{2}}\left(\frac{M_n}{M_m}\right)^{\frac{1}{4}}\right]^2, \tag{7}$$

where x_m, M_m, and $\mu_{0,m}$ are respectively the molar fraction, the molar mass, and the pure viscosity of the mth species. Note that, in the present study, we will assume that species have the same molar mass. A mixture viscosity can be defined as $\mu = \sum_m^N \mu_m$ and Wilke's formula for mixtures is recovered.

In addition to the viscous dissipation, the diffusion between species is of main importance in mixtures. The second line of Eq. (3) is a source term for each species, widely used to include forces in the lattice Boltzmann algorithm [26],

$$S_\alpha^m = \omega_\alpha\left[\frac{\boldsymbol{e}_\alpha-\boldsymbol{u}_m}{c_s^2}+\frac{(\boldsymbol{e}_\alpha\cdot\boldsymbol{u}_m)\boldsymbol{e}_\alpha}{c_s^4}\right]\cdot\boldsymbol{F}_m. \tag{8}$$

Here, $\boldsymbol{F}_m = \boldsymbol{F}_{\mathcal{D},m} + \boldsymbol{F}_{\mathrm{porous},m}$ where $\boldsymbol{F}_{\mathrm{porous},m}$ is the influence of the porous media, which will be detailed later, and $\boldsymbol{F}_{\mathcal{D},m}$ is the intermolecular friction force responsible for the diffusion between species, which can be expressed as

$$\boldsymbol{F}_{\mathcal{D},m} = -p\sum_{n=1}^{N}\frac{x_m x_n}{\mathcal{D}_{mn}}(\boldsymbol{u}_m-\boldsymbol{u}_n). \tag{9}$$

This force is a summation of binary interactions between species and depends on the species velocities difference, the Maxwell-Stefan diffusion coefficient $\mathcal{D}_{mn}$, molar fractions, and the total pressure given by Dalton's law $p = \sum_m^N p_m$, where the partial pressure is $p_m = \rho_m {c_s}^2$. The corresponding macroscopic governing equations, extensive details, and validations of the present multispecies lattice Boltzmann model can be found in Refs. [17,18].

In general, diffusion and advection are dealt with two separate mechanisms: one acting respectively on the species mass and the other acting on the mixture momentum. In contrast, by employing an intermolecular friction force, the diffusion and advection are coupled through the

species momentum. Diffusion and advection mechanisms are closely related in several physical phenomena, such as in the viscous fingering instability.

B. Porous medium in the lattice Boltzmann method

Simulating a flow through a porous medium at the pore scale requires a consequence amount of computational power and memory to obtain results for a large domain and a reasonable time frame. Instead, we consider an adequate scale where global variables such as the permeability of the porous medium can be defined. In the case of a single fluid, the Brinkman equation adds a drag force to the Stokes equations,

$$\nabla p = -\frac{\mu}{K}\boldsymbol{u} + \nabla \cdot \{\mu_e[\nabla \boldsymbol{u} + (\nabla \boldsymbol{u})^T]\}, \tag{10}$$

where p is the pressure, K is the permeability of the medium, $\boldsymbol{u}$ is the fluid velocity, and μ_e is the effective viscosity, which may not be equal to the fluid viscosity. The Brinkman equations are a convenient transition model between the Darcy regime ($K \ll L_{\text{ref}}^2 \mu/\mu_e$, with L_{ref} being the macroscopic characteristic length) and the Stokes regime ($K \gg L_{\text{ref}}^2 \mu/\mu_e$). The distinction between both regimes is possible via the Darcy number $\text{Da} = K/L_{\text{ref}}^2$ and the ratio μ/μ_e. One can show that in a Hele-Shaw cell, the flow is also governed by Darcy's law with an equivalent permeability of $b^2/12$ in the limit of low Reynolds number flow and $b/L_{\text{ref}} \to 0$, where b is the small gap width. It is to be noted that the dynamics of the viscous fingering is mainly governed by the Darcy equation [1]. Therefore, the Stokes term is not of primary importance, and the effective viscosity is taken equal to the fluid viscosity. Indeed, most of the literature only considers Darcy's equations. The latter equations correctly describe flows in Hele-Shaw cells and simple porous media, whereas Darcy-Brinkman's equations are often used as a transition model between porous flow and Stokes flow, such as in the case of fractured porous media.

Now we consider a homogeneous porous medium and a zone where the viscosity varies greatly. Under suitable assumptions, the flow follows a one-dimensional Darcy's law, and the pressure differential from both sides of the fictional interface as a result of a virtual displacement of δx reads [1]

$$\delta p = (p_{\text{left}} - p_{\text{right}}) = (\mu_{\text{right}} - \mu_{\text{left}})U/K\delta x. \tag{11}$$

If the total net pressure δp is positive, then any small displacement will amplify, resulting in an instability. From this simple argument, the instability mechanism is driven by the viscosity difference on either side of the interface. If the displaced fluid is more viscous than the displacing ($\mu_{\text{right}} > \mu_{\text{left}}$), then the configuration is unstable. In contrast ($\mu_{\text{right}} < \mu_{\text{left}}$), any small interface perturbation will be damped, and the configuration is stable.

How to model a porous medium in the lattice Boltzmann framework is an open subject, and different methodologies have been presented in various publications [27–33]. The two main strategies are based on a different approach. The first one can be interpreted as a particular boundary condition, and it ensures a local description of the medium by imposing a weighted bounce-back scheme on each mesh. This strategy is known as the gray lattice Boltzmann (GLBM) scheme [27,28,34]. The other strategy is less specific to the LBM framework and mimics the porous medium by adding a drag force to the governing equations. This latter methodology will be used for this study and will be further detailed hereafter. However, some numerical comparisons of both of these strategies can be found in Ref. [17], who have shown that the Brinkmann and the GLBM approaches would give similar results for the present viscous fingering instability.

In this section, we briefly present how to model the porous medium within a lattice Boltzmann framework. As described earlier, we seek an average view of the porous medium, and the equivalent target macroscopic equation is Darcy(-Brinkman)'s equation. In the Brinkman force (BF) model, the porous medium resistance is included explicitly through a drag force in the lattice Boltzmann

equation, e.g., [13,29–33]. We follow here a similar approach, and the forcing term is written as

$$\boldsymbol{F}_{\text{porous},m} = -\frac{\mu_m}{K}\boldsymbol{u}_m. \tag{12}$$

This strategy is local and has a negligible computational cost since we already implement a source term because of the intermolecular friction forces. As mentioned in Refs. [35–37], the numerical permeability depends lightly on the viscosity. This nonphysical variation can be alleviated by keeping the so-called magic number Λ constant (see Refs. [29,35–38]). We use the multiple relaxation times (MRT) collision model with $\Lambda = 3/16$ corresponding to $s_q = 8\frac{2-1/\tau_m}{8-1/\tau_m}$, where s_q refers to the relaxation time of the odd order moments [17]. The macroscopic equations described in Ref. [18] are thus supplemented by the porous drag force Eq. (12), and it is possible to simulate both Darcy and Stokes regimes. Since most of the literature deals with Darcy's law, we choose to focus on this regime. Consequently, we select a small Darcy number such that Darcy terms are predominant compared to the Stokes terms. More details regarding the influence of the Darcy number can be found in the Appendix.

III. NUMERICAL SIMULATIONS

A. Viscous fingering with two species

The viscous fingering instability occurs when a less viscous fluid invades a more viscous fluid. In the case of miscible fluids, if the interface between fluids is sharp enough, finger-like patterns emerge and grow, exhibiting complex dynamics. Following the literature, dimensionless parameters are defined, such as the log-viscosity ratio, the Péclet number (ratio of the advective transport rate and the diffusive transport rate), and the Darcy number:

$$R = \ln\left(\frac{\mu_{0,2}}{\mu_{0,1}}\right), \quad \text{Pe} = \frac{UL_{\text{ref}}}{\mathcal{D}_{12}}, \quad \text{Da} = \frac{K}{{L_{\text{ref}}}^2}, \tag{13}$$

where U is the injected velocity and L_{ref} is the reference length. Following Ref. [7], the characteristic scales are based on the convective length L_{ref} taken as the height of the domain, and the reference time is $t_{\text{ref}} = L_{\text{ref}}/U$. If $R < 0$, the invading fluid is more viscous than the resting fluid, and the interface is always stable. On the other hand, if $R > 0$, the invading fluid is less viscous than the resting fluid, and the interface between the two fluids may be unstable. The number of fingers increases with both the Péclet number and the ratio R. We recall that the relation between the pure viscosity and the species is given by Eq. (7). The influence of different parameters on the instability is studied. First, we present the numerical configuration employed to simulate the viscous fingering instability. The early times of the instability are compared with results from linear stability analysis. For intermediate times, we focus on the evolution of the mixing length induced by the fingering. The effects of the Péclet number are highlighted.

1. Numerical configuration

In the following simulations, the fluid consists of two species having equal molar masses. The resting mixture is composed of molar fractions $x_1 = 0.1$ and $x_2 = 0.9$ and these are swapped for the injected mixture ($x_1 = 0.9$, $x_2 = 0.1$). The domain considered is two dimensional and we impose periodicity at the top and bottom boundaries. At the left and right boundaries, a constant velocity condition equal to U is applied for both species. In the lattice Boltzmann method, a convenient system of units called lattice units (lu) is commonly employed. In this system, the time and space steps are set equal to 1. Conversion factors and nondimensional numbers are then used to compare the simulation with experimental or other numerical results. All the presented quantities are expressed in this system unless otherwise stated. Each simulation is initialized with an almost

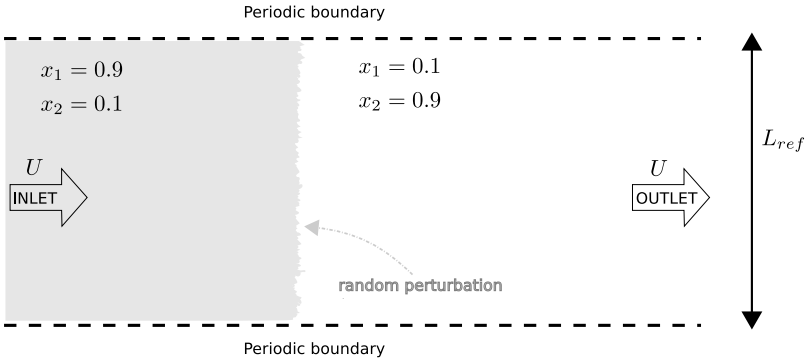

FIG. 1. Sketch of the initial configuration and boundary conditions.

sharp interface with a small perturbation so as to trigger the instability,

$$x_1(x, y, t = 0) = \frac{0.9 + 0.1}{2} + (0.1 - 0.9)\left[0.5 \times \mathrm{erf}\left(\frac{x - 0.1}{\sqrt{t_0}}\right) + r(y) \times \exp\left(\frac{-(x - 0.1)^2}{t_0}\right)\right], \tag{14}$$

$$x_2(x, y, t = 0) = 1 - x_1(x, y, t = 0), \tag{15}$$

where the function r returns a random number which is uniformly distributed in the interval $[0, 10^{-5}]$, and the same seed is used for the pseudorandom generator in each simulation. We set $t_0 = 10^{-6}$ to avoid strong gradients. The initial total pressure is computed from Darcy's law for the total mixture

$$p(x, y, t = 0) = p_{\mathrm{ref}} + (1 - x)\frac{\mu_1(x) + \mu_2(x)}{K}U, \tag{16}$$

with a unity reference pressure, and the distribution functions are initialized at their equilibrium values. A sketch of the numerical configuration is displayed in Fig. 1.

The viscous fingering instability is simulated here using a two-dimensional domain, and we may question what it implies. In Ref. [39], Oliveira and Meiburg discover a nonlinear mechanism called inner splitting, which is specific to the three-dimensional visous fingering instability. However, according to Homsy and Zimmerman [9], the nonlinear mechanisms found in two-dimensional persist in three dimensions, and for long times the evolution of the fingers remains unchanged from two dimensions. In particular, global variables, such as the mixing length, do not dramatically change from two-dimensional to three-dimensional simulations [10]. This suggests that two-dimensional simulations are sufficient to capture much of the essential physical features of viscous fingering. We also make a few additional assumptions. The porous medium is assumed to be isotropic, and the permeability is given by a scalar value. Viscous fingering in anisotropic media is studied utilizing linear stability analysis in Ref. [40]. The flow is more stabilized when the ratio of longitudinal to transverse anisotropic permeability is increased. Similarly, we only consider molecular diffusion, and we do not take into account the (anisotropic) dispersion caused in the flow at the pore scale since a general Taylor dispersion model is not known. Tan and Homsy [6] find from a linear stability analysis that the flow is more stable when the ratio of longitudinal to transverse anisotropic dispersion is decreased. With these assumptions, we will be able to compare our results with classical literature.

A fine spatial discretization is required in order to resolve all the length scales of the instability accurately, especially at high Péclet numbers. Preliminary simulations are performed to find the appropriate grid spacing. Three square grids are considered with different resolutions corresponding to the number of vertical lattice nodes $n_y = 1000, 2000, 4000$ where L_{ref} is kept constant. The initial

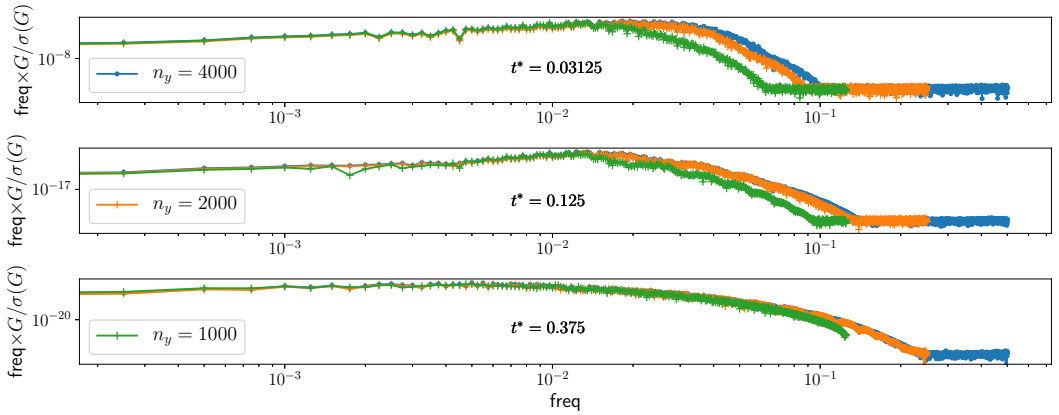

FIG. 2. Power spectral density at different times t^* for different resolutions equivalent to blue, $n_y = 4000$; orange, $n_y = 2000$; and green, $n_y = 1000$. $G = \hat{x}\hat{x}^\dagger$ where $\hat{x}^\dagger$ is the conjugate of the Fourier coefficients $\hat{x}$. G is normalized by its variance: $\sigma(G)$.

random perturbation is based on the grid where $n_y = 1000$, and interpolations are used for higher resolutions. Otherwise stated, we set

$$R = 3 \ (\mu_{0,2} \approx 20\mu_{0,1}), \quad \text{Pe} = 5000, \ \text{Da} = 6.25 \times 10^{-8}, \tag{17}$$

$$\text{Re}_{0,1} = \frac{U L_{\text{ref}} \rho_{\text{ref}}}{\mu_{0,1}} = 10, \ \text{Ma} = \frac{U}{c_s} = \sqrt{3} \times 10^{-3}. \tag{18}$$

With this specific value of Mach number, the inlet velocity is equal to 10^{-3} lu. This corresponds to a low Reynolds flow in the Darcy regime at a moderate Péclet number and viscosity ratio. We recall that two different systems of units are defined. There is the lattice unit system, where the time and space step are equal to 1, and the physical system. Nonetheless, all the dimensionless numbers are equal for either system of units.

For each resolution at different times, we carry out a fast Fourier transform (FFT) of the fingers. In particular, we take a slice of the domain where the mean molar fraction along the transverse direction is included in the interval [0.11, 0.89]. Afterward, we average along the longitudinal direction and apply a FFT to obtain the spectrum of the interface deformation according to the y-axis spatial frequency as plotted in Fig. 2. Results for different resolutions are compared at the same nondimensional time,

$$t^* = \frac{t}{t_{\text{ref}}} = \frac{tU}{L_{\text{ref}}}. \tag{19}$$

For short times, the lowest resolution corresponding to $n_y = 1000$ is not able to resolve the high frequencies of the instability. As the time progresses, larger structures appear and are captured by three resolutions, but for $n_y = 1000$ the amplitude of the fingers is slightly overpredicted at $t^* = 0.375$. Resolutions corresponding to $n_y = 2000$ and $n_y = 4000$ give equivalent results, suggesting that the main length scales of the instability are sufficiently well resolved. Nonetheless, we point out that global quantities such as the mean molar fraction or the mixing length are less sensitive to the resolution and can be adequately captured even with a very coarse grid. These results are in agreement with the linear stability analysis of a steep initial profile made in Ref. [7]. At the initial time $t = 0$, an analytical dispersion curve can be obtained, and the cutoff wave number is found to be equal to $R\text{Pe}/4 = 3750$, corresponding to a wave-length of 0.0017 for $\text{Pe} = 5000$ and $R = 3$. With a resolution of 0.001, the grid $n_y = 1000$ is inadequate for the present Péclet number. We will use mainly two resolutions, which correspond to two different lattice sizes. $n_y = 4000$ is employed

to capture all the small scales accurately at early times, and the aforementioned cutoff wave length is resolved with 6.7 points per wave length. In addition, a lower resolution equivalent to $n_y = 2000$ is chosen for simulations dedicated to intermediate times so as to reduce the computational cost. Indeed, a longer domain is needed to observe the development of the instability since the instability is convected at the injected velocity. Unfortunately, a formulation of the lattice Boltzmann scheme in the reference frame moving with the velocity of the injected fluid is not trivial and requires the use of rectangular lattices, which are beyond the scope of this work (see, for instance, Refs. [41–43]).

The study will be divided into two parts: early times and intermediate times. For early times, we will compare our results with the literature where the concentration goes down to zero. This is not possible with the present model since a tangible amount of species has to be modeled. The molar fractions of the invading mixture are therefore set to $x_1 = 0.999$, $x_2 = 0.001$ and are swapped for the displaced mixture. For intermediate times, molar fractions 0.9 and 0.1 are sufficient to obtain the global behavior of the instability with a coarse grid.

2. Early times

At early times, the interface between the two mixtures spreads because of diffusion and starts to deform. At the very beginning, the flow is linearly unstable, and perturbations grow exponentially. The onset of fingers is explored by many authors using linear stability analysis [1,2,6–8,40]. The Darcy equation, the continuity equation, and the transport equation for the concentration are linearized. A dispersion equation is later solved to compute the growth rate of the perturbation. An analytical solution is only known for the initial time, and numerical methods have then to be employed. Linear stability analysis can also be directly performed in the lattice Boltzmann framework (see Refs. [44,45]); however, this approach is still in its infancy and is only applied to simple single fluid flows. In this study, we carry out nonlinear simulations with the aforementioned lattice Boltzmann model and compute the growth rate of the perturbation *a posteriori*. The present approach has the advantage of avoiding the development of another tool and is valid for the whole instability including the nonlinear stage. The molar fractions can be decomposed into a base state x_m^0 and a perturbative component x_m',

$$x_m(\boldsymbol{x}, t) = x_m^0(\boldsymbol{x}, t) + x_m'(\boldsymbol{x}, t). \tag{20}$$

We assume that the perturbation can be expressed in the form of

$$x_m'(\boldsymbol{x}, t) = x_m'(\boldsymbol{x}) \exp(\sigma t) \tag{21}$$

where σ is the growth rate of the perturbation. The dispersion curves are obtained by applying a fast Fourier transform (FFT) along the transverse axis:

$$x_m'(\boldsymbol{x}, t) = x_m^0(\boldsymbol{x}, t) - x_m(\boldsymbol{x}, t) \tag{22}$$

$$\hat{x}(x, k, t) = \mathrm{FFT}_y(x_m'(\boldsymbol{x}, t)) \tag{23}$$

$$a(k, t) = ||\hat{x}(x, k, t)||_2 = \sqrt{\int \hat{x} \cdot \hat{x}^\dagger dx} \tag{24}$$

$$\sigma(k, t) = \frac{d \ln(a(k, t))}{dt}, \tag{25}$$

where $\hat{x}^\dagger$ is the complex conjugate of $\hat{x}$, k is the wave number, and we choose a time step sufficiently small such that the growth rate can be considered as constant between two derivation steps. a represents a measure in the Fourier space of the amplification of the perturbed molar fraction. Only relevant growth rates are of interest, consequently the growth rates of perturbations whose amplitudes are less than $10^{-4} \times \max_{\forall k}(a(k, t))$ are filtered out. The perturbative components are computed by subtracting the components from the nonlinear perturbed solution to the components from the base state. This base state is obtained by simulating the same conditions with no initial

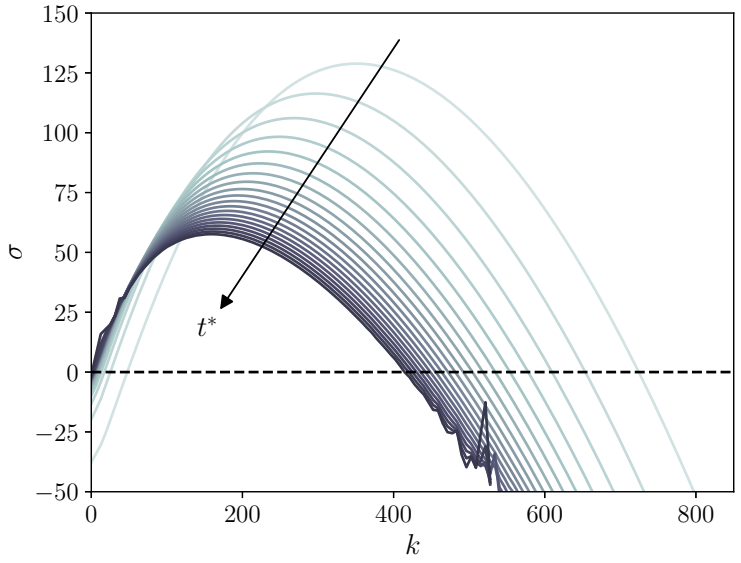

FIG. 3. Dispersion curve for Pe = 2000 at various times from $t^* = 0.005$ to $t^* = 0.1$ with a time step of $\Delta t^* = 0.05$ between each curve. The color gradient of the lines denotes the time evolution. ($n_x = 4000$, $n_y = 4000$).

perturbation. No finger emerges in this case. Therefore, two simulations with and without initial perturbations are performed for each case studied.

Figure 3 shows the growth rates computed from Eq. (25). Thus, at early times, the linear development of the instability is well captured by the proposed method. The growth rate decreases in time. The most dangerous wave number ($k_{\max}$) corresponding to the largest growth rate as well as the threshold (first wave number at which $\sigma = 0$) and the cutoff (k_c) (last wave number at which $\sigma = 0$) wave numbers are reduced as the instability progresses, resulting in widening fingers.

In Fig. 4, the growth rate for different Péclet numbers at $t^* = 0.01$ and $t^* = 0.1$ is compared with the results from Ref. [7] where a linear stability analysis using a self-similar quasi-steady-state

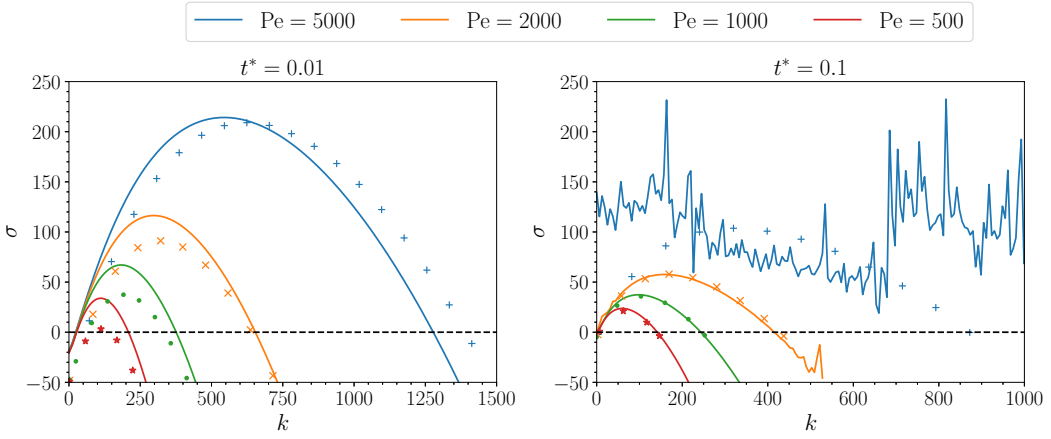

FIG. 4. Dispersion curves for $R = 3$ at $t^* = 0.01,\ 0.1$ with different Péclet values. Lines stand for the simulation and the symbols are data obtained by a linear stability analysis from Ref. [7]. ($n_x = 4000$, $n_y = 4000$).

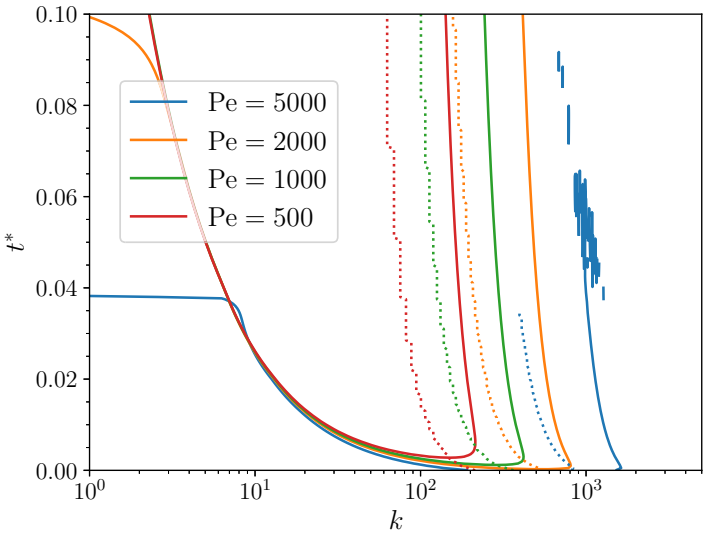

FIG. 5. Neutral stability curves ($\sigma = 0$) for different Péclet numbers at $R = 3$ according to the time and the wave number. Dashed lines represent the most dangerous wave number $k_{\max}$. For $t^* > 0.035$ and Pe = 5000, nonlinear interactions take place and the most dangerous wave number is not plotted ($n_x = 4000$, $n_y = 4000$).

approximation is employed. A close overall agreement is found for the different Péclet numbers. The discrepancies between quasi-steady-state approximation linear stability analyses and nonlinear simulations are more pronounced at early times ($t^* = 0.01$) as already pointed out in Refs. [6,8]. The previous authors mention that, for short times, initial value problem and nonmodal analysis are closer to nonlinear simulations results. In particular, the quasi-steady-state assumption means that the resulting eigenvalue problem is solved with a frozen base state. This assumes that the growth rate of the perturbations to be much faster than the rate of change of the base state. As expected, excellent agreement is found at latter times ($t^* = 0.1$) for Pe < 5000. For Pe $= 5000$, nonlinear interactions occur and the perturbation can no longer be described by Eq. (21). Note that the linear description of the instability could be still valid at the time $t^* = 0.1$ if the flow is initially perturbed by only one wave number instead of being excited on the whole spectrum. This more accurate strategy required to run a simulation (two precisely for the perturbed and nonperturbed cases) for each wave number of interest. This becomes rapidly impractical if one wants to study the time evolution of the instability as the relevant wave numbers where $\sigma > 0$ depends on time and shift toward smaller wave numbers as time progresses.

Diffusion acts as a stabilization factor by smoothing perturbations and heading to a homogeneous mixture. Hence, as shown in Fig. 4, the instability is more dominant at higher Péclet numbers. A lower fluid dispersion expands the range of unstable wave numbers and increases the growth rate. The cutoff wave number increases with the Péclet number, whereas it has a very limited influence on the threshold wave number. This can be easily seen on neutral stability curves (contours of $\sigma = 0$) plotted in Fig. 5. The differences from the bell-shaped curve are due to the nonlinear interactions. The area above the neutral curve defines the region of instability whereas the area below the neutral curve corresponds to a negative (stable) growth rate. As described earlier, this region increases with the Péclet number. The minimum (t^*_{crit}, k_{crit}) on the neutral curves is the limit that below the perturbation is stable. It is interesting to note that we can also define a critical Péclet number Pe_{crit}, and its value depends on the time. For Pe $= 500$ and Pe $= 1000$, the flow is initially stable and then becomes unstable at latter times, whereas for Pe $= 5000$ at $t^* = 0$ the flow seems unstable throughout. For very short times, the growth of the interface caused by large diffusion (low Péclet numbers) surpasses the exponential growth of the perturbation. This also implies that, as expected,

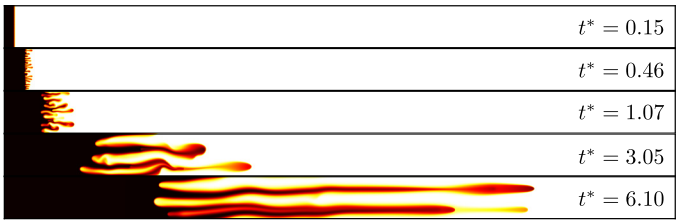

FIG. 6. Instability development for $R = 3$, Pe $= 2000$ at $t^* \approx 0.15,\ 0.46,\ 1.07,\ 3.05,\ 6.10$. The whole domain ($n_x = 8192,\ n_y = 512$) is plotted. The color map (black-red-yellow-white) represents the variation of the molar fraction from $x_1 = 0.9$ to $x_1 = 0.1$. The same scaling is used for both x and y axes.

there is a minimal critical Péclet number, such as the flow is always stable when the diffusion is large enough. Nonetheless, more simulations with smaller time steps and various Péclet numbers should be performed to quantity this phenomenon and dismiss transient numerical artifacts, especially for large Péclet numbers. When plotted in a logarithm scale according to the times, straight lines are obtained for the most dangerous and cutoff wave numbers, as we can infer from Fig. 5. For a log viscosity ratio $R = 3$, the most dangerous wave number decreases rapidly and then slows as $k_{\max} \sim t^{*-0.26}$ compared to the cutoff wave number where $k_c \sim t^{*-0.36}$. All of these observations are consistent with the results presented in Ref. [7], and this shows that the present model is adequate to study the linear stage of the instability.

3. Intermediate times

Figure 6 shows a sequence of snapshots of a simulation at $R = 3$, Pe $= 2000$. At early times ($t^* \leqslant 0.1$), the sharp interface diffuses and begins to deform. This stage is called the linearly unstable regime, and linear stability analysis tools are suitable to describe the instability as shown previously. Afterward, many thin fingers develop, and strong linear interactions take place as seen at $t^* = 0.46, 1.07, 3.05$. These can be identified as spreading, shielding, fading, and coalescence. A brief definition of these phenomena found in the literature is given hereafter. By spreading, we refer to the process whereby one finger is slightly ahead of others. The finger grows very quick, and the gradient steepens between the finger and the surrounding more viscous fluid. The finger may then widen at the tip and shield the growth of the smaller neighboring fingers. Few thin fingers fade and diffuse in the ambient fluid, resulting in a region of intermediate viscosity. The coalescence phenomenon describes the merging of two or more fingers together. This mechanism is fundamental since it is the merging of smaller fingers in the nearby dominant finger that keeps supplying the latter with less viscous fluid, as we can see from the third snapshot of Fig. 6. The present dynamics of the simulation is rich, displaying all major mechanisms. For higher Péclet numbers, the flow also exhibits more complex behaviors such as tip splitting, when a finger splits into two at the tip and side branching when a finger splits at its side [1,2]. These fascinating interaction mechanisms lead globally to a coarsening of the fingers in the transverse direction and growth of the fingers in the longitudinal direction. The number of fingers and the intensity of these interactions increase with the Péclet number and the log-viscosity ratio. Finally, for $t^* > 3$, the few remaining fingers grow at a constant rate. At the very late times (not observed here; see the discussion in Ref. [2]), the fingers should mix with the ambient fluid and are convected at a given speed close to the injected velocity. The length of the fingers should stay roughly the same since the interface is diffuse enough to smooth out the viscosity and concentration gradients.

A convenient way to describe the global dynamic is by observing the evolution of the mixing length, which is defined here as the distance where the transverse average molar fraction is included between 0.89 and 0.11. In Fig. 7, the mixing length multiplied by the Péclet number is represented with a logarithmic scale according to $t^* \times$ Pe for various Péclet numbers at $R = 3$. With this particular scaling, all the curves are superimposed. Two different regimes are clearly visible. In

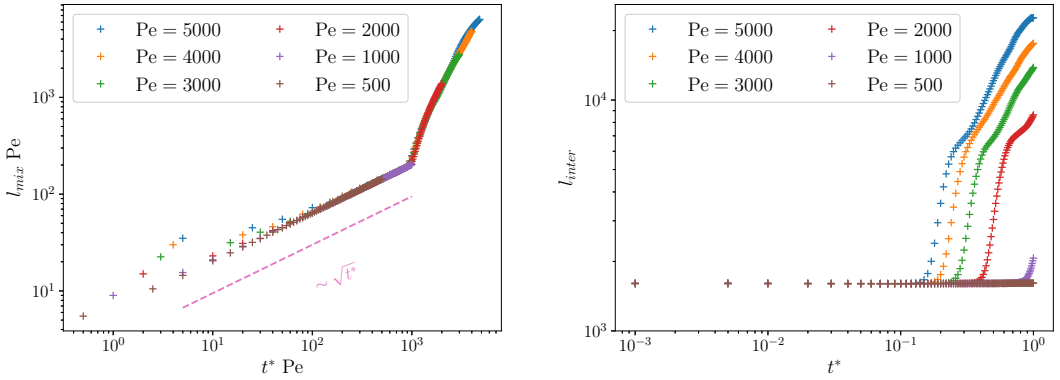

FIG. 7. Temporal evolution of the mixing length (left) and the interfacial length (right) for different Pe ($n_x = 4000$, $n_y = 2000$, and $R = 3$).

the first regime, the diffusion dominates the growth of the mixing length, which is proportional to $\sqrt{t^*}$ as in the case of no viscosity contrast ($R = 0$, pure diffusion). Afterward, a transition regime may occur, depending on the Péclet number. In the second regime, the growth of the mixing length is linear in time, suggesting that the advection now dominates. As the instability is more intense, the transition time decreases, and the duration of this transition increases. During this transition, strong nonlinear interactions occur, as can be seen in Fig. 6 at $t^* \approx 0.46, 1.07, 3.05$.

We would like to make a few remarks concerning the mixing length. This quantity is not appropriate if one wants to determine the time when fingers become visually perceptible. Actually, when the perturbations start to interfere nonlinearly, such as at $t^* \approx 0.1$ for Pe $= 2000$, the deformation of the interface is imperceptible. Fingers become noticeable later during the diffusion-dominated regime and before the advection-dominated regime, as shown in Fig. 8. A better measurement of

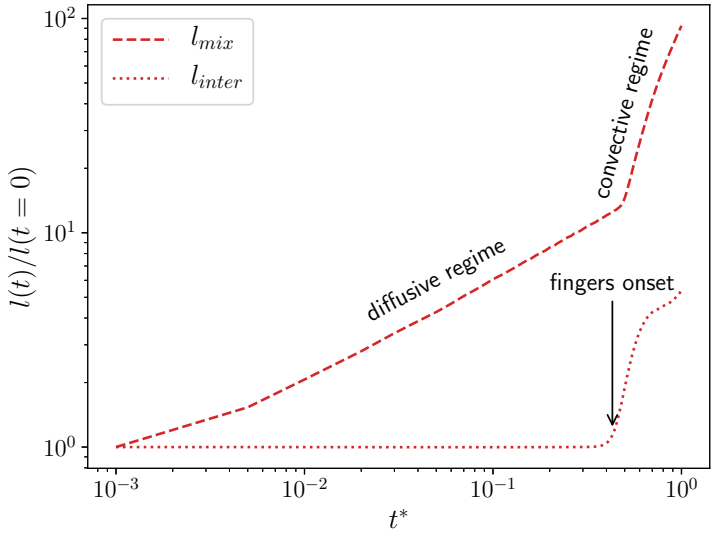

FIG. 8. Temporal evolution of the normalized interfacial and mixing lengths at Pe $= 2000$ ($n_x = 4000$, $n_y = 2000$, and $R = 3$).

the visible onset of the fingers is given by a sudden growth of the interfacial length,

$$l_{\text{inter}}(t) = \iint [(\partial x_1/\partial x)^2 + (\partial x_1/\partial y)^2]^{\frac{1}{2}} dxdy, \tag{26}$$

caused by the surge of the transverse gradient of the molar fraction [46]. In any case, both indicators increase earlier and reach larger values for higher Péclet numbers, revealing a more intense instability.

B. Viscous fingering with three species

1. Physical context

In the previous results, the relation between the viscosity and the concentration is given by Eq. (7) and not the exponential dependence usually found in the literature (see, e.g., Refs. [1,6,7]). However, the calculated growth rates are in good agreement with Ref. [7], as shown in Fig. 4. This could be expected as, for binary mixture, Fick or Maxwell approaches for diffusion are equivalent, and for species having the same molecular mass, the mixture viscosity $\mu_1 + \mu_2$ has a similar shape as $\mu_{0,2}e^{-Rx_1}$. For a binary mixture with species having different molecular masses, the variation of the mixture viscosity according to the mixture composition is more complex, and it can be nonmonotonic; i.e., the maximum of the mixture viscosity can take place at intermediate molar fractions. The behavior of the instability is then much more complex. A linear stability analysis shows that all nonmonotonic viscosity profiles, irrespective of their end-point viscosities, become unstable [47]. This means that viscous fingering effectively occurs if the Péclet number is sufficiently high. Significant differences in the (nonlinear) development of fingers between monotonic and nonmonotonic viscosity profiles are explained in Ref. [48]. Due to the stable barrier in the nonmonotonic profile, fingers spread further in displacing fluid than in the displaced fluid. Moreover, Hota and Mishra [49] observe that three important parameters characterize the nonmonotonic viscosity profile, namely, endpoint viscosity contrast, maximum viscosity, and the concentration that maximizes the viscosity. In the favorable case, the instability could be triggered more rapidly when the maximum viscosity and concentration that maximize the viscosity are increased. For the present simulations, these parameters are not directly imposed but are related to the ternary diffusion mechanisms induced by the diffusion matrix Eq. (35).

More complicated configurations can happen in the case of reacting mixture $A + B \rightarrow C$ depending on the properties of the reactants and the product. The viscosity profile can be monotonic or nonmonotonic and changes in time according to the diffusion and reaction rates. Some phenomena are identical to those observed in the viscous fingering of a finite slice [46] because of the finite size of the chemical reaction zone. De Wit and other authors study numerically and experimentally the influence of the reaction on the viscous fingering instability; see Refs. [16,50–54]. Nonetheless, they do not focus on the diffusion involved by the reactants and the product of the chemical reaction. Most of the analyses assume a generalized Fick formulation with the same or a constant Fick diffusion coefficient for all species, which is generally incorrect. Finally, let us mention the pioneered work of Mishra *et al.* [55]. The advantage of the set of equations proposed in [55] is that they can mimic numbers of different cases from the influences of temperature to the influence of multiple species. In particular, the authors highlight different scenarios of viscous fingering in the case of a quickly diffusing component and a slowly diffusing component, which modifies the viscosity of the mixture. Each advection-diffusion equation is simulated with a constant Fick diffusion coefficient. Nevertheless, if we solely focus on ternary mixtures, a complete description of the ternary diffusion by the generalized Fick law should require at least four nonconstant Fick diffusion coefficients and two associated diffusive fluxes for each advection-diffusion equation, and the last species is deduced from the difference between the total mass of the mixture and the mass of the first two species [56].

Fick's law seems easier to manipulate and gives a direct relationship between the molar fluxes and the gradient of the molar fraction. Nonetheless, its application to three and more components has severe flaws and could lead to some misconceptions of mass transfer. A Maxwell-Stefan approach

to mass transfer, which is equivalent to the fiction forces introduced in the present model [Eq. (9)], is more adequate for three and more species, as we will explain below. The conceptual difference between these two formulations is that the Maxwell-Stefan approach assumes that difference of the diffusive fluxes (velocities) results in concentration differences, and on the other hand, the generalized Fick formulation deduces the diffusive fluxes from the concentration differences. The multicomponent Fick diffusion coefficient D should not be confused with the Maxwell-Stefan (also called binary) diffusion coefficients $\mathcal{D}$. For a mixture of two species, both coefficients are equivalent. For three components and more, a Fick-like formulation is still possible [see Eqs. (27)–(29) below], but it is often inadequate because the Fick diffusion coefficients are not as practical as the Maxwell-Stefan diffusion coefficients. First, four Fick diffusion coefficients are needed to describe a ternary mixture. These coefficients may be positive or negative, are usually nonsymmetric, and vary according to the mixture composition. Besides, D_{mn} has less physical meanings in that it does not reflect the *m*-*n* interactions, and their numerical values depend on the particular choice of component numbering. Finally, the multicomponent Fick diffusion coefficients have to be manipulated with great care since they depend on the choice of the associated fluxes. In contrast, the Maxwell-Stefan diffusion coefficients are symmetric positive. Their values can be computed from the kinetic theory of gases and are related to the physical interactions between molecules. For instance, if $\mathcal{D}_{mn} > \mathcal{D}_{mo}$, then there is more friction (collision) between the molecules of species m and o than between the species m and n. More details concerning the basics of multicomponent diffusion can be found in Ref. [56]. A correct description of a mixture composed of three and more species is of fundamental importance. Nontrivial effects can occur during the mixing, such as osmotic diffusion (diffusion of a species with a null concentration gradient), reverse diffusion (diffusion of a species in the same direction of its concentration gradient), and diffusion barrier (no species diffusion although the species has a nonzero concentration gradient). The present lattice Boltzmann scheme is valid whatever the number of species composing the mixture [18], and for this reason, it is a convenient tool to study the viscous fingering instability of a mixture of three species.

As we saw previously, the viscous fingering instability is governed by diffusion and viscosity. Unlike in binary mixtures where each species diffuses at an equal rate ($\mathcal{D}_{12} = \mathcal{D}_{21}$), in ternary mixtures the components can diffuse at different rates ($\mathcal{D}_{12} \neq \mathcal{D}_{13} \neq \mathcal{D}_{22}$). Also, multicomponent effects such as reverse diffusion, osmotic diffusion, and diffusion barrier may take place, and the overall diffusion dynamics become more complex. While in binary mixtures, we have $x_1 = 1 - x_2$ and $\nabla x_1 = -\nabla x_2$, and these constraints on the molar fractions in ternary mixtures are less strict: $x_1 + x_2 + x_3 = 1$ and $\nabla x_1 + \nabla x_2 + \nabla x_3 = \mathbf{0}$. As a consequence, since the viscosity depends on the mixture composition, the viscosity evolution could change significantly compared to the binary case. In this section, we will focus on a particular flow configuration in order to highlight the non-negligible effect of ternary mixtures. The case where viscous fingering instability is induced by reverse diffusion has, to our knowledge, not been investigated yet and is presented here. However, it is to be highlighted that the following simulations will be presented as a "numerical experiment" to demonstrate the importance of reverse diffusion rather than a real situation because experimental data with species satisfying the present conditions are, to our knowledge, not yet treated in the literature.

2. Numerical configuration

The numerical setup is very similar to the one for two species, but the invading and displaced fluids are here composed of different species. The mixture consists of three species in different quantities having equal molecular masses. The composition of the invading and displaced mixtures is given in Fig. 9. The molar fractions of the first and second components follow a similar steplike initial concentration profile, such as in the case of the binary mixture. Note that here the first component is less present than the second component in the invading mixture and *vice versa* in the displaced mixture. The third component is in equal amounts in both invading and displaced fluids. Before defining additional physical parameters, we would like to present how this ternary

Molar fractions	Invading fluid	Displaced fluid
x_1 (R)	0.1	0.45
x_2 (G)	0.45	0.1
x_3 (B)	0.45	0.45
RGB color		

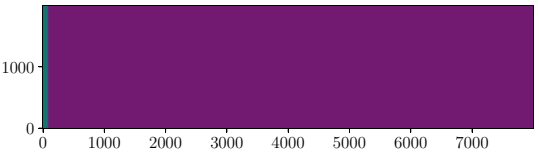

FIG. 9. Left: Composition of the invading and displaced mixtures. Right: Initial state of the computational domain.

mixture will be visualized. Each species is associated with a red-green-blue (RGB) color channel. With this strategy, one is able to deduce the mixture composition from one single color map similar to the case of a binary mixture. The color depicted in Fig. 9 corresponds to the RGB color mixing, coloring the invading fluid in a green-blue tone and the displaced fluid in purple. Therefore, in the following, the first, second, and third components will be referred respectively to as the red, green, and blue components.

The diffusion coefficients are set such as the blue component will be subject to reverse diffusion. This can be estimated by means of the generalized Fick formulation in the case of pure diffusion:

$$\boldsymbol{J}_2 = -c_t D_{22} \boldsymbol{\nabla} x_2 - c_t D_{23} \boldsymbol{\nabla} x_3, \tag{27}$$

$$\boldsymbol{J}_3 = -c_t D_{32} \boldsymbol{\nabla} x_2 - c_t D_{33} \boldsymbol{\nabla} x_3, \tag{28}$$

$$\text{and } \boldsymbol{J}_1 = -\boldsymbol{J}_2 - \boldsymbol{J}_3, \tag{29}$$

where $\boldsymbol{J}_m$ is the molar flux of component m and c_t is the total molar concentration. We want $\boldsymbol{J}_3 < \boldsymbol{0}$ and since $\boldsymbol{\nabla} x_3 = \boldsymbol{0}$ and $\boldsymbol{\nabla} x_2 = (<0, 0)^T$, we should have $D_{32} < 0$. We recall the definition of the generalized Fick diffusion coefficients:

$$D_{22} = \mathcal{D}_{23}(x_2 \mathcal{D}_{13} + (1 - x_2)\mathcal{D}_{23})/\hat{D} \tag{30}$$

$$D_{23} = x_2 \mathcal{D}_{12}(\mathcal{D}_{12} - \mathcal{D}_{23})/\hat{D}, \tag{31}$$

$$D_{33} = \mathcal{D}_{13}(x_3 \mathcal{D}_{12} + (1 - x_3)\mathcal{D}_{23})/\hat{D}, \tag{32}$$

$$D_{32} = x_3 \mathcal{D}_{12}(\mathcal{D}_{13} - \mathcal{D}_{23})/\hat{D}, \tag{33}$$

$$\text{with } \hat{D} = x_1 \mathcal{D}_{23} + x_2 \mathcal{D}_{13} + x_3 \mathcal{D}_{12}. \tag{34}$$

Hence, we should set $\mathcal{D}_{23} > \mathcal{D}_{13}$ in order to observe reverse diffusion. We choose the following diffusion matrix

$$\mathcal{D}_{mn} = \frac{L_{\text{ref}} U}{\text{Pe}}(0 \quad 1 \quad 0.1 \; 1 \quad 0 \quad 1 \; 0.1 \quad 1 \quad 0), \tag{35}$$

with $\text{Pe} = 5000$, $U = 2 \times 10^{-3}$lu, the Darcy number is unchanged, $\text{Da} = 6.25 \times 10^{-8}$, and the porous medium is simulated using the Brinkman force strategy. Pure viscosities are set based on $\text{Re}_{0,1} = 10$ and $R_{12} = \ln(\mu_{0,1}/\mu_{0,2}) = 0$, $R_{13} = \ln(\mu_{0,1}/\mu_{0,3}) = 3$. The red and green components which vary on either side of the miscible interface have the same pure viscosity, whereas the pure viscosity of the blue component present in equal amount in the domain is approximately 20 times lower. Compared to the binary case, the boundary conditions are modified. We still use the nonequilibrium bounceback, which prescribes for each species either a pressure or a velocity at boundary nodes. For a mixture composed of two species, we impose a velocity, and small changes of partial pressure (mixture composition) occur. In the case of three components, the variation of the mixture composition at boundaries compared to the initial target fluid becomes important, so we

FIG. 10. Snapshot of the viscous fingering induced by reverse diffusion at $t^* = 3$. A portion of the whole domain ($x = 4100$–4800, $y = 0$–2000) is plotted using the same aspect ratio for both x and y axes. The plot is rotated by 90°. The invading fluid is flowing from the bottom to the top of the figure.

choose to impose the pressure at both boundaries using Eq. (16) adapted for three species. One can note that this could introduce a slight decrease in the inlet velocity when simulation progresses, and thus the Péclet number should be interpreted carefully in the latter times.

Given the initial state pictured in Fig. 9, both invading and displaced mixtures have the same viscosity. Then, if the diffusion coefficients have all the same value, this reduces to a binary mixture as the first and second species are identical, and as expected, the flow is stable when both invading and displaced fluid viscosities are equal. However, if we set the diffusion matrix as in Eq. (35), fingers develop as pictured in Fig. 10, although the initial configuration is stable. This scenario was one of the possibities predicted in Ref. [55], and the dynamic of the instability is studied in two stages, as in the case of two species. First, we will focus first on the linear development of the instability at early times, then we explore the dynamic of the fingers at intermediate times.

3. Early times

Similarly to the two species case, dispersion curves are plotted using Eq. (25). As explained in Sec. III A 1, a fine grid ($n_x = 4000, n_y = 4000$) is employed to capture all the small scales accurately at early times. Other parameters are the same as stated in the previous section. We first observe in Fig. 11 that the three species have different growth rates. As we may infer from the diffusion coefficient $\mathcal{D}_{13}$ of Eq. (35), the instability is triggered by diffusion and the third (blue)

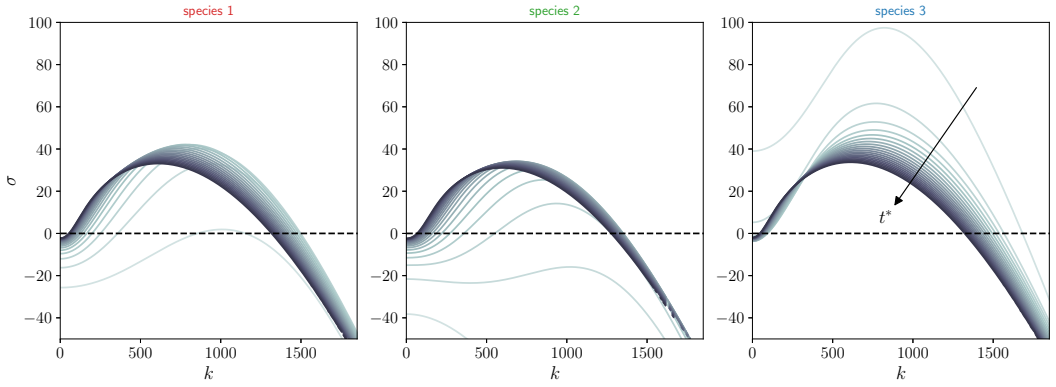

FIG. 11. Dispersion curve for each species at various times from $t^* = 0.005$ to $t^* = 0.1$ with a time step of $\Delta t^* = 0.05$ between each curve. The color gradient of the lines denotes the time evolution. ($n_x = 4000$, $n_y = 4000$).

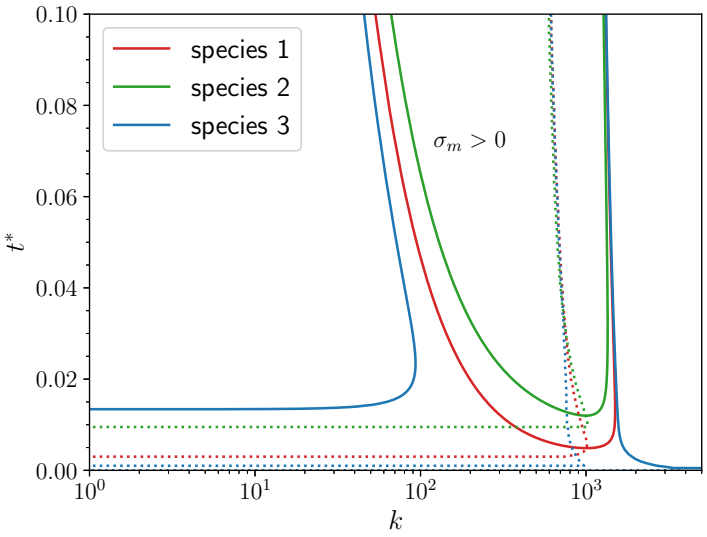

FIG. 12. Neutral stability curves ($\sigma_m = 0$) according to the time and the wave number. Dashed lines represent the most dangerous wave number $k_{\max}$.

component plays a peculiar role that will be explained in detail in the next section. The blue species exhibits a high and positive growth rate, which decreases as the time progresses like in the binary case. In contrast, the growth rate of the first and second species are first negative. The growth rate of the red species increases more rapidly than that of the green species and then both decline in the same way as the blue component. At identical times, the growth rates of first and second species are lower than that of the third (blue) species. This suggests that the blue species is actually the driving force of the the instability onset. Interestingly, the growth rate of all species seems to converge to the same value. In particular, for $t^* \geqslant 0.05$ the most dangerous and the cutoff wave numbers are very similar for the three species as visible in Fig. 12. Using a linear interpolation, we find $k_{\max}(t \gg 0) \approx 457$ and $k_c(t \gg 0) \approx 1220$, which is in the same order of magnitude as in the binary case for $\mathrm{Pe} = 5000$.

Although the linear approach of the early times predicts an equivalent growth rate for the three species, we will observe in the next section that the development of the fingers during intermediate times is different depending on the species.

4. Global dynamics

The global dynamics of the instability could be split into three distinct regimes:

Instability onset caused by reverse diffusion: $t^\star < 1$. The fingering is actually caused by the reverse diffusion as inferred from Figs. 13 and 14. At the beginning of the simulation, the blue and less viscous component is uniformly present. However, the blue component starts to diffuse from the displaced to the invading mixtures (osmotic diffusion) and keeps diffusing in the same direction as its concentration gradient (reverse diffusion: from low to high concentration) and against the main flow. The temporal evolution of the blue component mass fraction at the interface (Fig. 13) shows an initial decrease of the mass fraction due to the mass transfer of the blue component from the displaced fluid to the invading fluid. This decrease induces a lower viscosity of the invading fluid which creates a favorable situation for the viscous fingering instability. When the viscosity of the invading fluids becomes small enough, the instability begins: Fingers start to develop and counteract the decrease of the blue species at the interface of the invading and displacing fluids

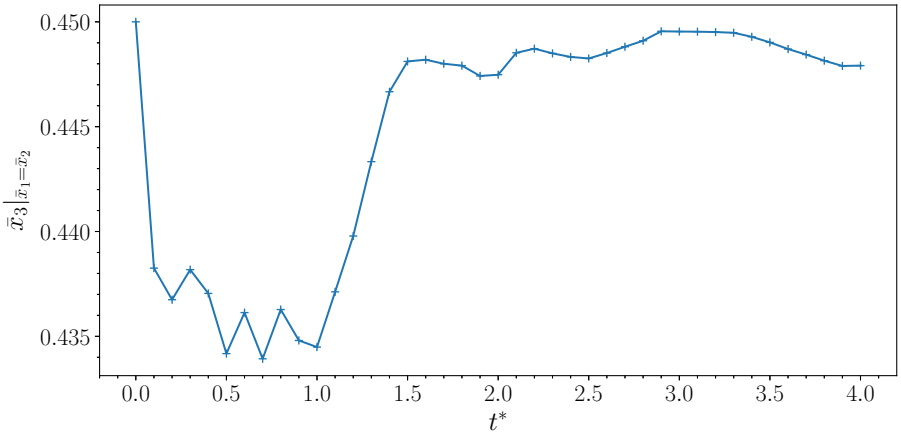

FIG. 13. Temporal evolution of the mass fraction of the blue component recorded at the interface.

(where $x_1 = x_2$). Indeed, as for the two-species case, an interfacial length could be defined for each component, and it starts to increase drastically from $t^\star = 1$ as seen in Fig. 15.

Diffusive regime: $1 \leqslant t^\star < 1.6$. Then, after $t^* = 1$, the growth of the initial fingers brings some blue component into the displaced fluid and an increase of the mean transverse concentration of the blue component at the interface is clearly visible. As in the two-species case, it is possible to define a mixing length associated with each species. For the red and green components, the mixing length corresponds to the distance where the transverse molar fraction is included between 0.11 and 0.44. On the other hand, there is no simple end point for the definition of the mixing length of the blue component since the minimal and maximum transverse average molar fraction changes dynamically because of the reverse diffusion and the development of the instability. For $t^\star < 1.6$, the mixing length is dominated by the diffusion, and the finger length remains smaller than the diffusion length, which evolves with $\sqrt{t^\star}$ (Fig. 15).

Convective regime: $t^\star \geqslant 1.6$. At $t^* = 1.6$, the convective behavior of the instability starts to be visible. The length of the fingers becomes larger than the diffusion length. The mixing length is dominated by the growth of the fingers and is now proportional to $t^\star$ (Fig. 15). A concentration plateau for the blue component appears until the breakthrough of the fingers takes place, increasing the mean transverse concentration of the blue component in the upstream direction and decreasing it in the downstream direction, as seen in Fig. 14 at $t^* = 2.1, 3.8$. Notice that the effective viscosity ratio is lower and makes the instability less intense compared to the binary case with the same Péclet number. We recall that the mixture viscosity is computed *a posteriori*, whereas only partial viscosities are employed in the model. At this point in the instability development, the interface between the invading and displaced fluids is significantly deformed. In consequence, the mean transverse concentration and viscosity are no longer appropriate to describe the variation of the concentrations and viscosities.

These three regimes depict the global dynamics from the invading and displaced fluids' point of view. However, some local descriptions could be made to describe further the dynamics at the component level. Indeed, fingering refers usually to the deformation of the interface between the invading and displaced fluids, but the dynamic of each component constituting the mixture varies greatly. Despite the fact that at the end of the linear stage of the instability the growth rate of the three species become similar, the dynamic of the nonlinear stage is different for each species. The blue-colored fingers highlight the displacement of the blue component because of the instability, but the contour-plots indicate also some variations of the interface for the first (red) species. In Fig. 16, the molar fraction of each species is plotted. The right figure shows that some fingers are composed of a very high concentration of the blue component. Counterfingers, which move from the right

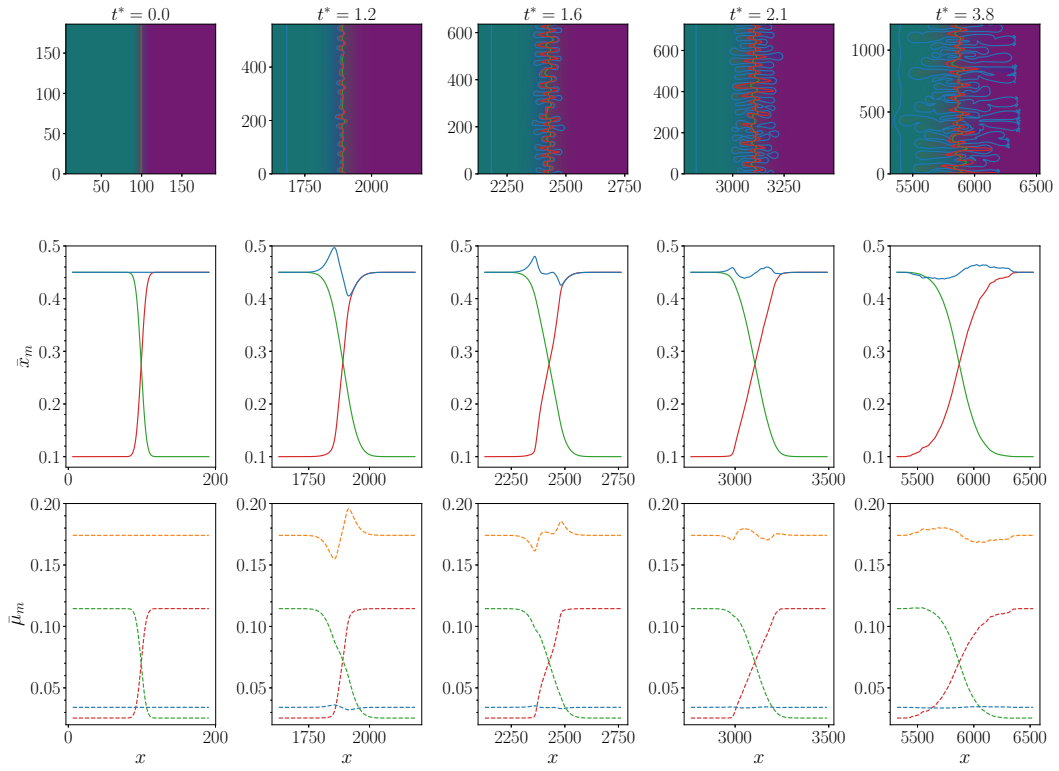

FIG. 14. Evolution at different times of the mean molar fraction over the transverse direction, continuous lines, and the mean partial viscosity over the transverse direction, dashed lines. Viscosities are normalized by the pure viscosity $\mu_{0,1}$. Red, first species; green, second species; blue, third species. Orange stands for the mean mixture viscosity over the transverse direction.

to the left, have a minimal molar fraction of $x_3 = 0.34$. We underline that reverse diffusion still occurs, tends to reinforce the fingers, and limits the development of counterpropagating fingers of low concentration. The interface of the red component is also significantly deformed. The invading fluid penetrates the displaced fluid primarily through the low-viscosity fingers caused by the blue

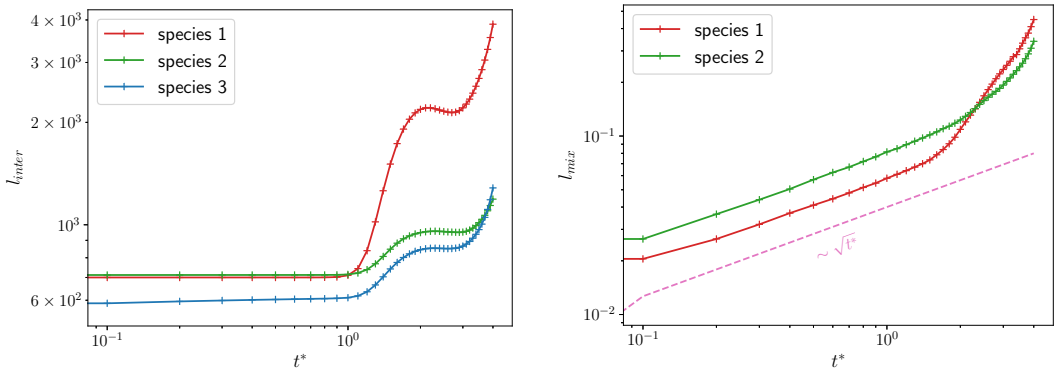

FIG. 15. Temporal evolution of the interfacial length (left) and mixing length (right).

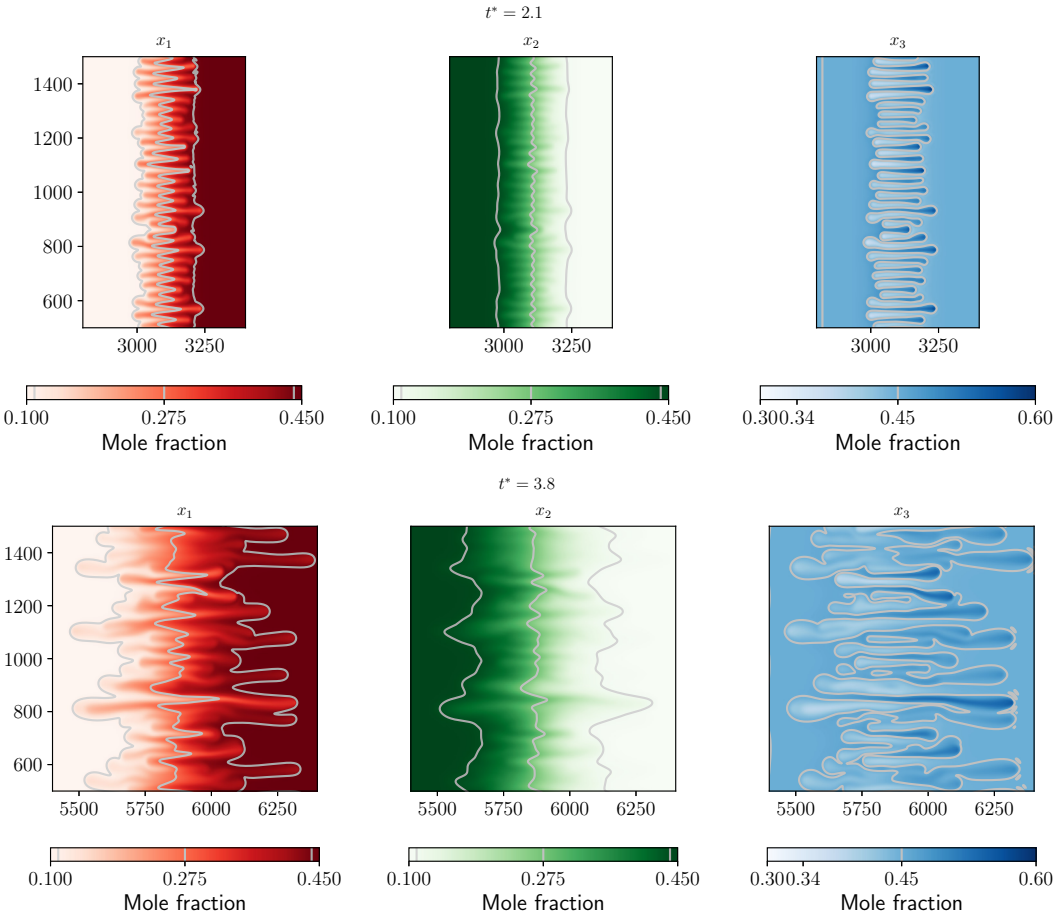

FIG. 16. Color map of the molar fraction for each species. Portion of the domain ($n_x = 8000$, $n_y = 2000$).

component and avoids the zone of high viscosity. In consequence, small fingers of low concentration of the red component develop. One can notice that, in contrast, the interface of the green component seems symmetrically diffuse. This phenomenon can be explained via the diffusion matrix Eq. (35). Since $\mathcal{D}_{13} < \mathcal{D}_{12}$, the red component diffuses predominantly in the green component compared to the blue component, that is why small fingers of low concentration of the red component are visible in fingering caused by the blue component. In other words, the red component is dragged along by the fingers of the blue component. Concerning the green component, we have $\mathcal{D}_{12} = \mathcal{D}_{23}$, and it diffuses in both species equitably.

With the numbers of different possible configurations of viscosities and diffusion coefficients, a complete parametric study is out of the scope of the present work. Nonetheless, some dramatic changes due to subtle effects have been highlighted when considering complex diffusion in multi-component flows.

IV. CONCLUSION

The interactions between two (or three) miscible components are described by a miscible lattice Boltzmann model. The core ingredients of the instability are related to the molecular diffusion and the viscosity discrepancy, or more specifically for the aforementioned lattice Boltzmann model:

intermolecular friction forces and partial viscosities. Generally, the instability occurs when a less viscous fluid displaces a more viscous fluid in a porous medium. The viscous fingering is studied first in the case of a binary mixture. At early times in the linear regime, the growth rate of the perturbation is calculated for different Péclet numbers. The growth rate, as well as the most dangerous and the cutoff numbers, increase with the Péclet number. A good agreement is found with a linear stability analysis where a quasi-steady-state approximation is used. For intermediate times when strong nonlinear interactions take place, the development of the instability is described globally through the mixing length. A high Péclet number leads to more intense instability. Two regimes are visible. The growth of the mixing length is dominated first by diffusion and then by convection. The comparison with the literature, quantitatively for early times and qualitatively for intermediate times agrees well. This is very encouraging and gives much credence to the lattice Boltzmann model proposed in Ref. [18]. Indeed, with a different approach based on the lattice Boltzmann method, we accurately recover the physics of the binary viscous fingering instability.

The results of ternary mixtures have shown that the reverse diffusion (and multicomponent diffusion effects) could be one of the essential elements of the viscous instability. Indeed, we pointed out that two fluids of the same viscosity but composed of three species may generate a fingering instability depending on the composition of the mixture and the diffusion coefficients, whereas this configuration is stable for binary mixtures. Therefore, the study of the viscous fingering instability of three and more components should be performed with a complete description of multicomponent diffusion in order to take into account this phenomenon. More generally, the use of generalized Fick's law with the assumption of constant diffusion coefficients for viscous fingering simulations of three and more species excludes some nontrivial diffusion interactions, which may cause an unstable configuration. From these results, control of the instability could be possible by adding a particular component in a mixture, which could switch the instability on or off through diffusion dynamics only. This latter point should be the purpose of further studies with numerical and experimental investigations.

ACKNOWLEDGMENTS

The authors acknowledge the referees for their constructive remarks and criticisms which have led to noticeable improvements of the paper. This work was granted access to the HPC resources of CINES under the allocations 2019-A0072A10636 and 2020-A0092A10636 made by GENCI (Grand Equipement National de Calcul Intensif).

APPENDIX: EFFECTS OF DARCY'S NUMBER

In the present model, the porous media is included explicitly via the forcing term Eq. (12). The resulting macroscopic equations presented in Ref. [18] have to be supplemented by the aforementioned porous drag force. Consequently, it is not possible to separate the effect of the Darcy term from that of the Stokes term [leading to the Brinkman equation (10)] in the computational LMB model. A small Darcy number $\mathrm{Da} = 6.25 \times 10^{-8}$ is selected (that is equivalent to $K = 1$ in the lattice unit system, but any other small Darcy number could be chosen) such as the contribution of the Darcy term is preponderant, and this makes it possible to compare results with the literature where Darcy's law is used.

The role of the Darcy number, that is to say, the importance of the viscous stresses, on the development of the viscous fingering instability could be non-negligible, although most of the literature is based on the use of Darcy's law. In Ref. [57], Logvinov *et al.* show that viscous forces acting in the plane of a Hele-Shaw cell plates can influence the width of viscous fingers for miscible fluids. Nagel and Gallaire [58] observe that the in-plane stresses accounted by the Brinkman model decrease the growth rate for high wave numbers, and the resulting linear stability analysis agrees better with experimental observations for radial viscous nonmiscible viscous fingering. This effect

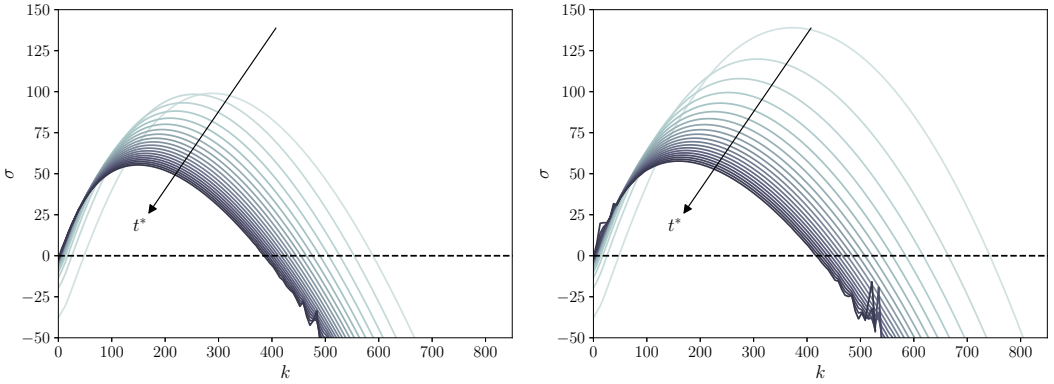

FIG. 17. Dispersion curve for $\mathrm{Da} = 10^{-6}$ (left) and $\mathrm{Da} = 10^{-9}$ (right), $\mathrm{Pe} = 2000$ at various times from $t^* = 0.005$ to $t^* = 0.1$ with a time step of $\Delta t^* = 0.05$ between each curve. The color gradient of the lines denotes the time evolution.

on the grow rate is also noticeable with the present model as shown in Fig. 17 at the very beginning of the instability.

Unfortunately, the computational model and the chosen parameters in this study limit the range of exploitable Darcy numbers. Stable simulations are currently obtained for $10^{-9} \leqslant \mathrm{Da} \leqslant 10^{-6}$. This range of Darcy numbers is too narrow to explore this effect thoroughly and should require subsequent study.

[1] G. M. Homsy, Viscous fingering in porous media, Annu. Rev. Fluid Mech. **19**, 271 (1987).
[2] J. S. Nijjer, D. R. Hewitt, and J. A. Neufeld, The dynamics of miscible viscous fingering from onset to shutdown, J. Fluid Mech. **837**, 520 (2018).
[3] D. Lasseux and F. J. Vamdés-Parada, On the developments of Darcy's law to include inertial and slip effects, C. R. Mec. **345**, 660 (2017).
[4] S. Hill, Channeling in packed columns, Chem. Eng. Sci. **1**, 247 (1952).
[5] P. G. Saffman and G. I. Taylor, The penetration of a fluid into a porous medium or Hele-Shaw cell containing a more viscous liquid, Proc. R. Soc. London, Ser. A **245**, 312 (1958).
[6] C. T. Tan and G. M. Homsy, Stability of miscible displacements in porous media: Rectilinear flow, Phys. Fluids **29**, 3549 (1986).
[7] S. Pramanik and M. Mishra, Effect of Péclet number on miscible rectilinear displacement in a Hele-Shaw cell, Phys. Rev. E **91**, 033006 (2015).
[8] T. K. Hota, S. Pramanik, and M. Mishra, Nonmodal linear stability analysis of miscible viscous fingering in porous media, Phys. Rev. E **92**, 053007 (2015).
[9] W. B. Zimmerman and G. M. Homsy, Three-dimensional viscous fingering: A numerical study, Phys. Fluids A **4**, 1901 (1992).
[10] A. Riaz and E. Meiburg, Three-dimensional miscible displacement simulations in homogeneous porous media with gravity override, J. Fluid Mech. **494**, 95 (2003).
[11] B. Jha, L. Cueto-Felgueroso, and R. Juanes, Quantifying mixing in viscously unstable porous media flows, Phys. Rev. E **84**, 066312 (2011).
[12] R. Holme and D. H. Rothman, Lattice-gas and lattice-Boltzmann models of miscible fluids, J. Stat. Phys. **68**, 409 (1992).
[13] N. Rakotomalala, D. Salin, and P. Watzky, Miscible displacement between two parallel plates: BGK lattice gas simulations, J. Fluid Mech. **338**, 277 (1997).

[14] G. Liu and Z. Guo, Pore-scale study of the non-linear mixing of fluids with viscous fingering in anisotropic porous media, Commun. Comput. Phys. **17**, 1019 (2015).
[15] T. Lei, X. Meng, and Z. Guo, Pore-scale study on reactive mixing of miscible solutions with viscous fingering in porous media, Comput. Fluids **155**, 146 (2017).
[16] T. Lei and K. H. Luo, Pore-scale study of dissolution-driven density instability with reaction $a + b \rightarrow c$ in porous media, Phys. Rev. Fluids **4**, 063907 (2019).
[17] L. Vienne, Simulation of multi-component flows by the lattice Boltzmann method and application to the viscous fingering instability, Ph.D. thesis, Conservatoire national des arts et metiers (CNAM), Paris, France, 2019, https://tel.archives-ouvertes.fr/tel-02447641.
[18] L. Vienne, S. Marié, and F. Grasso, Lattice Boltzmann method for miscible gases: A forcing-term approach, Phys. Rev. E **100**, 023309 (2019).
[19] L.-S. Luo and S. S. Girimaji, Theory of the lattice Boltzmann method: Two-fluid model for binary mixtures, Phys. Rev. E **67**, 036302 (2003).
[20] P. Asinari, Semi-implicit-linearized multiple-relaxation-time formulation of lattice Boltzmann schemes for mixture modeling, Phys. Rev. E **73**, 056705 (2006).
[21] P. Asinari, Multiple-relaxation-time lattice Boltzmann scheme for homogeneous mixture flows with external force, Phys. Rev. E **77**, 056706 (2008).
[22] S. Arcidiacono, I. V. Karlin, J. Mantzaras, and C. E. Frouzakis, Lattice Boltzmann model for the simulation of multicomponent mixtures, Phys. Rev. E **76**, 046703 (2007).
[23] N. Sawant, B. Dorschner, and I. V. Karlin, Consistent lattice Boltzmann model for multicomponent mixtures, J. Fluid Mech. **909**, A1 (2021).
[24] X. Shan, X. Yuan, and H. Chen, Kinetic theory representation of hydrodynamics: A way beyond the Navier-Stokes equation, J. Fluid Mech. **550**, 413 (2006).
[25] J. O. Hirschfelder, C. F. Curtiss, and R. B. Bird, *Molecular Theory of Gases and Liquids*, 2nd ed. (John Wiley & Sons, New York, 1964).
[26] Z. Guo, C. Zheng, and B. Shi, Discrete lattice effects on the forcing term in the lattice Boltzmann method, Phys. Rev. E **65**, 046308 (2002).
[27] S. D. Walsh, H. Burwinkle, and M. O. Saar, A new partial-bounceback lattice Boltzmann method for fluid flow through heterogeneous media, Comput. Geosci. **35**, 1186 (2009).
[28] J. Zhu and J. Ma, An improved gray lattice Boltzmann model for simulating fluid flow in multi-scale porous media, Adv. Water Resour. **56**, 61 (2013).
[29] I. Ginzburg, Consistent lattice Boltzmann schemes for the Brinkman model of porous flow and infinite Chapman-Enskog expansion, Phys. Rev. E **77**, 066704 (2008).
[30] Z. Guo and T. S. Zhao, Lattice Boltzmann model for incompressible flows through porous media, Phys. Rev. E **66**, 036304 (2002).
[31] N. S. Martys, Improved approximation of the Brinkman equation using a lattice Boltzmann method, Phys. Fluids **13**, 1807 (2001).
[32] M. A. A. Spaid and F. R. Phelan, Lattice Boltzmann methods for modeling microscale flow in fibrous porous media, Phys. Fluids **9**, 2468 (1997).
[33] P. Grosfils, J. P. Boon, J. Chin, and E. S. Boek, Structural and dynamical characterization of Hele–Shaw viscous fingering, Philos. Trans. R. Soc. London, Ser. A **362**, 1723 (2004).
[34] H. Yoshida and H. Hayashi, Transmission–reflection coefficient in the lattice Boltzmann method, J. Stat. Phys. **155**, 277 (2014).
[35] L. Talon, D. Bauer, N. Gland, S. Youssef, H. Auradou, and I. Ginzburg, Assessment of the two relaxation time lattice-Boltzmann scheme to simulate stokes flow in porous media, Water Resour. Res. **48**, W04526 (2012).
[36] S. Khirevich, I. Ginzburg, and U. Tallarek, Coarse- and fine-grid numerical behavior of MRT/TRT lattice-Boltzmann schemes in regular and random sphere packings, J. Comput. Phys. **281**, 708 (2015).
[37] I. Ginzburg, Comment on an improved gray lattice Boltzmann model for simulating fluid flow in multi-scale porous media: Intrinsic links between LBE Brinkman schemes, Adv. Water Resour. **88**, 241 (2016).
[38] D. d'Humières and I. Ginzburg, Viscosity independent numerical errors for lattice Boltzmann models: From recurrence equations to "magic" collision numbers, Comput. Math. Appl. **58**, 823 (2009).

[39] R. M. Oliveira and E. Meiburg, Miscible displacements in Hele-Shaw cells: Three-dimensional Navier–Stokes simulations, J. Fluid Mech. **687**, 431 (2011).
[40] M. Norouzi and M. R. Shoghi, A numerical study on miscible viscous fingering instability in anisotropic porous media, Phys. Fluids **26**, 084102 (2014).
[41] M. Bouzidi, D. d'Humières, P. Lallemand, and L.-S. Luo, Lattice Boltzmann equation on a two-dimensional rectangular grid, J. Comput. Phys. **172**, 704 (2001).
[42] L. A. Hegele Jr., K. Mattila, and P. C. Philippi, Rectangular lattice-Boltzmann schemes with BGK-collision operator, J. Sci. Comput. **56**, 230 (2012).
[43] C. Peng, H. Min, Z. Guo, and L.-P. Wang, A hydrodynamically-consistent MRT lattice Boltzmann model on a 2d rectangular grid, J. Comput. Phys. **326**, 893 (2016).
[44] E. Vergnault, O. Malaspinas, and P. Sagaut, A lattice Boltzmann method for nonlinear disturbances around an arbitrary base flow, J. Comput. Phys. **231**, 8070 (2012).
[45] J. M. Pérez, A. Aguilar, and V. Theofilis, Lattice Boltzmann methods for global linear instability analysis, Theor. Comput. Fluid Dyn. **31**, 643 (2016).
[46] M. Mishra, M. Martin, and A. D. Wit, Differences in miscible viscous fingering of finite width slices with positive or negative log-mobility ratio, Phys. Rev. E **78**, 066306 (2008).
[47] O. Manickam and G. M. Homsy, Stability of miscible displacements in porous media with nonmonotonic viscosity profiles, Phys. Fluids A **5**, 1356 (1993).
[48] O. Manickam and G. M. Homsy, Simulation of viscous fingering in miscible displacements with non-monotonic viscosity profiles, Phys. Fluids **6**, 95 (1994).
[49] T. K. Hota and M. Mishra, Non-modal stability analysis of miscible viscous fingering with non-monotonic viscosity profiles, J. Fluid Mech. **856**, 552 (2018).
[50] S. H. Hejazi, P. M. J. Trevelyan, J. Azaiez, and A. D. Wit, Viscous fingering of a miscible reactive a + b → c interface: A linear stability analysis, J. Fluid Mech. **652**, 501 (2010).
[51] Y. Nagatsu and A. D. Wit, Viscous fingering of a miscible reactive a + b → c interface for an infinitely fast chemical reaction: Nonlinear simulations, Phys. Fluids **23**, 043103 (2011).
[52] L. A. Riolfo, Y. Nagatsu, S. Iwata, R. Maes, P. M. J. Trevelyan, and A. D. Wit, Experimental evidence of reaction-driven miscible viscous fingering, Phys. Rev. E **85**, 015304(R) (2012).
[53] V. Sharma, S. Pramanik, C.-Y. Chen, and M. Mishra, A numerical study on reaction-induced radial fingering instability, J. Fluid Mech. **862**, 624 (2019).
[54] S. Priyanka and A. D. Wit, Influence of the Péclet number on reactive viscous fingering, Phys. Rev. Fluids **5**, 014004 (2020).
[55] M. Mishra, P. M. J. Trevelyan, C. Almarcha, and A. D. Wit, Influence of Double Diffusive Effects on Miscible Viscous Fingering, Phys. Rev. Lett. **105**, 204501 (2010).
[56] R. Taylor and R. Krishna, *Multicomponent Mass Transfer* (John Wiley & Sons, New York, 1993).
[57] O. A. Logvinov, O. E. Ivashnyov, and N. N. Smirnov, Evaluation of viscous fingers width in Hele-Shaw flows, Acta Astronaut. **67**, 53 (2010).
[58] M. Nagel and F. Gallaire, A new prediction of wavelength selection in radial viscous fingering involving normal and tangential stresses, Phys. Fluids **25**, 124107 (2013).